RSC Advances

ROYAL SOCIETY OF CHEMISTRY

PAPER

View Article Online
View Journal | View Issue

Cite this: *RSC Adv.*, 2026, **16**, 21307

Enhanced electrochemical and thermoelectric performance of bacterial cellulose-based composite aerogels *via* multi-component reinforcement

Qi Xiao,†*[ac] Enhao Xie,†[a] Zhe Gao,[d] Yuhan Wang,[a] Wen Chen,[a] Wei Fan,[c] Jahongir Akhmedov[e] and Ulugbek Gulbaev*[b]

Received 5th February 2026
Accepted 17th April 2026

DOI: 10.1039/d6ra01008c

rsc.li/rsc-advances

Flexible wearable electronics demand multifunctional materials with robust mechanical properties, high conductivity, and sensing capabilities. However, existing bacterial cellulose (BC)-based aerogels suffer from poor mechanical stability and limited electrical performance. Here, we report a synergistic, multi-component reinforcement strategy for fabricating high-performance BC-based composite aerogels. By incorporating sodium alginate (SA) as a toughening modifier and integrating dual conductive polymers (poly(3,4-ethylenedioxythiophene) (PEDOT) and polyaniline (PANI)), we construct an ionically cross-linked network *via* Ca^{2+} chelation. The optimized aerogel (BC : PEDOT = 2 : 1, 30% SA, 4% PANI) demonstrates remarkable multifunctional performance: a specific capacitance of 37.09 F g^{-1} with 98.3% retention after 10 000 cycles, superior thermoelectric properties (Seebeck coefficient: 0.7 mV K^{-1}, electrical conductivity: 4.5 S cm^{-1}, power factor: 220.5 μW m^{-1} K^{-2}), and stable pressure-responsive behavior (18.5 mV and 6.8 μA at 5 kPa). The composite aerogel exhibits good mechanical properties, with a stress of up to 9.6 kPa at 100% compressive deformation after 100 cycles. The Ca^{2+}-mediated ionic cross-linking significantly enhances mechanical robustness compared to pristine BC aerogels, while the synergistic combination of PEDOT and PANI creates continuous electron-transport pathways. This work demonstrates that rational design of multi-component systems can overcome the traditional trade-off between mechanical and electrical properties in BC-based materials, offering a promising approach for next-generation flexible electronics, including self-powered sensors and wearable energy storage devices.

Introduction

The rapid development of flexible wearable electronics urgently demands materials combining high conductivity, mechanical robustness, and multifunctional sensing capabilities. However, existing BC-based aerogels exhibit poor mechanical properties and limited electrical performance.[1] Bacterial cellulose (BC) is a biosynthetic nanofiber material.[2] Its unique three-dimensional network structure confers high porosity, excellent biocompatibility, degradability, and mechanical properties, making it an ideal matrix for constructing high-performance composite aerogels.[3,4] It demonstrates strong potential for application, particularly in the field of flexible electronic textiles, such as pressure-sensing smart wearables and body-heat-powered fabrics.[5] Such applications require synergistic properties, including high flexibility, bend resistance, and stable electrical performance.[6,7] However, the inherent insulating nature of BC significantly limits its direct use in electronic devices, necessitating functionalization through doping or compositing with conductive materials. To enhance the conductivity and thermoelectric conversion efficiency of BC-based composite aerogels, effective doping with conductive polymers has emerged as a key strategy.[8,9] Among these, poly(3,4-ethylenedioxythiophene) (PEDOT) is favored for its high electrical conductivity and excellent environmental stability.[10,11] It can be incorporated into the BC network *via in situ* polymerization to form a π–π-conjugated system. This endows the composite with both high mechanical strength and high electrical conductivity, making it suitable for flexible electronic substrates. Previous studies have prepared BC-

---

[a] *School of Textile Garment and Design, Suzhou University of Technology, Changshu, Jiangsu 215500, China. E-mail: xiaoqi223638@163.com*

[b] *School of Textile Materials and Technology, Jizzakh Polytechnic Institute, Uzbekistan. E-mail: ulugbekgulboev94@gmail.com*

[c] *Key Laboratory of Functional Textile Materials and Products, Ministry of Education, Xi'an Polytechnic University, Xi'an 710048, China*

[d] *School of Textile Science and Engineering, Tiangong University, Tianjin 300387, China*

[e] *Tashkent Institute of Textile and Light Industry, Uzbekistan*

† Qi Xiao and Enhao Xie are the co-first authors.

PEDOT aerogels by combining PEDOT with BC, thereby significantly enhancing the system's carrier transport efficiency.[12,13] Furthermore, polyaniline (PANI), valued for its high conductivity and environmental stability, is frequently blended with BC.[14] By adjusting reaction parameters, such as the oxidant molar ratio and dopant concentration, the synergistic optimization of both conductivity and capacitance properties in the composite material can be achieved. However, simple blends of single conductive polymers with BC still face limitations—the resulting aerogels exhibit suboptimal overall thermoelectric performance and insufficient mechanical properties. After repeated bending in textile devices, conductivity can decrease by over 30%, failing to meet the demands of practical applications.[15]

To address these issues, multi-component synergistic reinforcement strategies have emerged as a practical approach to enhance the performance of composite aerogels. Herein, a high-performance bacterial cellulose-based composite aerogel was fabricated using a synergistic multicomponent strategy. SA was incorporated as a toughening modifier and integrated with two complementary conductive polymers (PEDOT and PANI) to construct an ionic crosslinking network *via* Ca^{2+} chelation, followed by freeze-drying. The microstructure, electrochemical energy storage characteristics, and energy-harvesting performance of the composite aerogels were systematically investigated. Notably, the rationally designed ionic crosslinking system, which achieves a true synergistic reinforcement effect, was based on SA/Ca^{2+} coordination and synergistically coupled with a binary conductive polymer framework. Moreover, compositional tuning of the multicomponent system enables an optimal balance among diverse performance, yielding comprehensive properties that significantly surpass those of conventional counterparts.

Experimental

Materials

Bacterial cellulose (BC, 0.8%), Foshan Sailuna Technology Co., Ltd; poly(3,4-ethyldioxothiophene) aqueous dispersion (PEDOT, 1.5%), Shenzhen Yilai Technology Co., Ltd; sodium alginate (SA, 90%), polyaniline (PANI, 98%), polyvinyl alcohol (type 1788, hydrolyzation degree: 87.0–89.0%), anhydrous calcium chloride (99.99%), potassium hydroxide (KOH, 99.99%), from Shanghai McLean Biochemical Technology Co., Ltd.

Preparation

BC and PEDOT dispersions were blended at mass ratios of 1 : 1, 2 : 1, 3 : 1, 4 : 1, and 5 : 1. The mixture was stirred magnetically at room temperature for 1 h, then ultrasonicated for an additional 1 h to ensure uniformity. The blended solution was then freeze-dried at −40 °C for 48 h to obtain BC-PEDOT aerogels, which were named BC1-PEDOT1, BC2-PEDOT1, BC3-PEDOT1, BC4-PEDOT1, and BC5-PEDOT1.

The BC : PEDOT ratio was fixed at 2 : 1, and SA was incorporated at varying mass fractions. SA content was defined as $m_{SA}/(m_{BC} + m_{PEDOT})$, with values of 10%, 20%, 30%, 40%, and 50%. The mixture was stirred magnetically for 1 h. Subsequently, calcium chloride ($CaCl_2$) solution—containing 3% $CaCl_2$ relative to the mass of SA—was added, and the mixture was further stirred for 1 h. The mixture was then transferred to a constant-temperature bath maintained at 25 °C and left undisturbed for 6 h to ensure complete gelation. Finally, the hydrogel was freeze-dried at −40 °C for 48 h to yield BC2-PEDOT1-SA composite aerogels with distinct SA mass fractions, designated as BC2-PEDOT1-SA10, BC2-PEDOT1-SA20, BC2-PEDOT1-SA30, BC2-PEDOT1-SA40, and BC2-PEDOT1-SA50.

Based on the optimal SA mass fraction determined in the previous step, the effect of polyaniline (PANI) content on BC2-PEDOT1-SA30-PANI aerogels was further investigated. BC, PEDOT, SA, and PANI were mixed. PANI content was defined as $m_{PANI}/(m_{BC} + m_{PEDOT} + m_{SA})$, with values of 2%, 3%, 4%, 5%, and 6%. The mixture was stirred magnetically for 1 h, then ultrasonically dispersed for 1 h. The mixture was then freeze-dried at −40 °C for 48 h to obtain BC2-PEDOT1-SA30-PANI composite aerogels containing different mass fractions of PANI, which were named as BC2-PEDOT1-SA30-PANI2, BC2-PEDOT1-SA30-PANI3, BC2-PEDOT1-SA30-PANI4, BC2-PEDOT1-SA30-PANI5, BC2-PEDOT1-SA30-PANI6. The preparation flowchart is shown in Fig. 1.

Preparation of gel electrolyte: 6 g of PVA was weighed and dissolved in 50 mL of deionized water. The solution was stirred at room temperature for 15 min, then transferred to a 90 °C water bath, and stirred for 60 min, until it became transparent. It was defoamed in a vacuum drying oven. 6 g of KOH was weighed and dissolved in 10 mL of deionized water. The KOH solution was added dropwise to the PVA solution under heating and stirring. After completing the addition, stirring was continued for 30 min, then heating was stopped. The mixture was allowed to cool naturally to room temperature and continuously stirred to obtain a homogeneous, transparent PVA/KOH gel electrolyte.

Assembly of flexible supercapacitors. A symmetric two-electrode supercapacitor was assembled using the as-prepared BC-based conductive composite aerogel as freestanding electrodes. Two electrodes with comparable mass and identical geometric area were cut from the same aerogel monolith and then separated by a PVA/KOH gel electrolyte. The sandwich electrode was encapsulated to obtain a symmetrical aerogel capacitor for electrochemical measurements.

Characterization and measurements

Morphological characterization of the aerogels was performed using a Sigma 300 thermal-field-emission scanning electron microscope (SEM). The test voltage is 5 kV, and gold-spraying treatment is performed before the test. Functional groups of the aerogels were identified and characterized using a Nicolet 5700 Fourier Transform Infrared Spectrometer (FTIR). The resolution is 4 cm^{-1}. Scan count is 32. The wavenumber range is 4000–500 cm^{-1}. The elemental composition and relative elemental content of aerogels were examined using a Nexsa X-ray photoelectron spectrometer (XPS). The compression stress–strain relationship of the aerogels was tested using

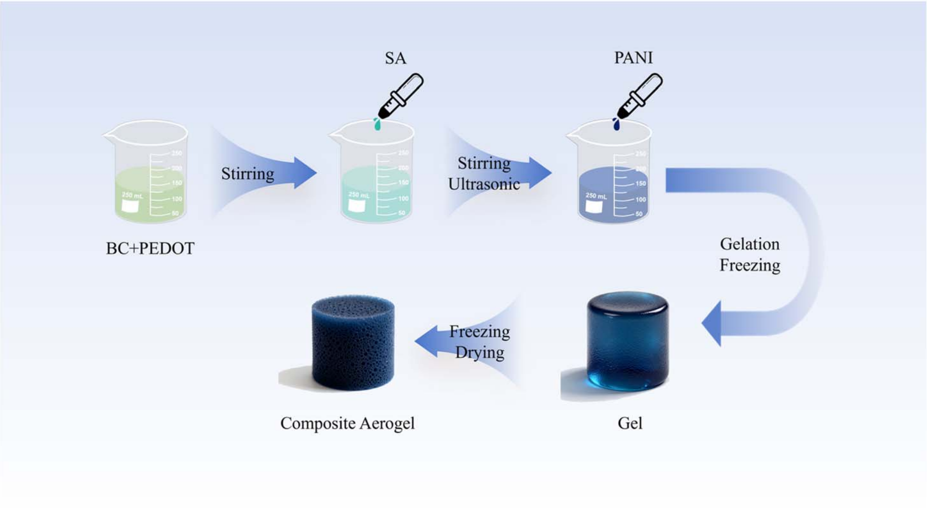

Fig. 1 The preparation flowchart.

a universal testing machine (HT2402), with a compression rate of 3 mm min^{-1}.

An X-ray diffraction tester (D/max-2200/PC) with Cu-Ka radiation ($\lambda = 0.154$ nm) was used to characterize the crystal structure of the aerogels. The X-ray diffraction patterns of the aerogels were recorded in reflection mode by scanning 10–80° with a step size of 0.05° and a scan rate of 5° min^{-1}. And the crystallinity index is determined by the following equation.

$$I = \frac{I_{002} - I_{\mathrm{a}}}{I_{002}} \times 100\% \tag{1}$$

where I is the crystallinity index of the aerogel, %; I_{002} is the peak intensity of the (002) crystal plane, and I_{a} is the peak intensity of the amorphous region.

The thermal analysis of the aerogels was performed using a STA449F3C thermogravimetric analyzer. The samples were heated in a nitrogen atmosphere from 30 to 600 °C, with a heating rate of 10 °C min^{-1}. The specific surface area and pore size distribution of the aerogels were determined using the static adsorption method with the ASAP2020 Surface Area and Pore Analyzer. A 0.193 g sample was tested at 77.35 K with N_2 as the adsorbate to obtain N_2 adsorption–desorption isotherms.

Electrochemical performance testing

Electrochemical testing of the assembled flexible supercapacitor was conducted using a CHI760E electrochemical workstation. CV (Cyclic Voltammetry) tests were conducted within a working potential window of 0–0.8 V at scan rates of 5, 10, 20, 50, and 100 mV s^{-1}. EIS (Electrochemical Impedance Spectroscopy) tests were performed over a frequency range of 1–100 kHz with an AC amplitude of 5 mV. The point at which the EIS curve intersects the X-axis corresponds to the equivalent series resistance. GCD (Galvanostatic Charge–Discharge) tests were conducted at a current density of 1A g^{-1} 10 000 charge–discharge cycles were conducted to evaluate the cycling stability of the aerogel. The gravimetric specific capacitance, energy density, and power density of the supercapacitors were calculated using the following eqn (2)–(4).

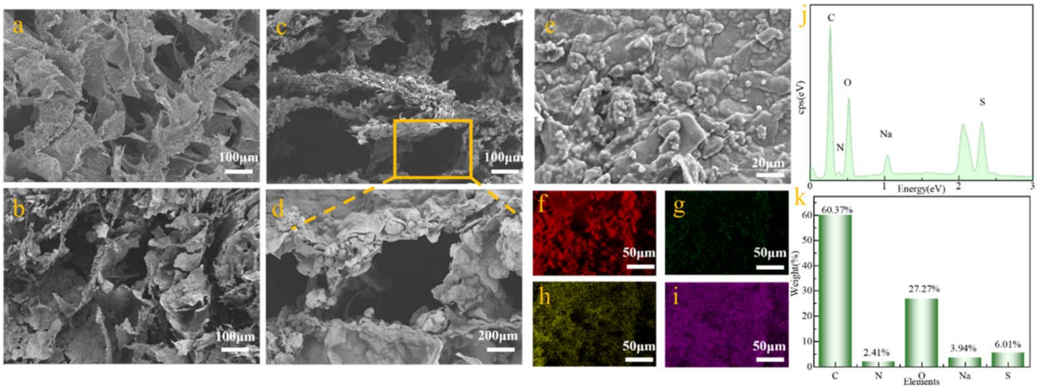

Fig. 2 (a) SEM image of BC-PEDOT aerogel, (b) SEM image of BC-PEDOT-SA aerogel, (c)–(e) SEM images of BC-PEDOT-SA-PANI aerogel, (f)–(i) corresponding EDX mappings of elemental C, N, Na, and S in BC-PEDOT-SA-PANI aerogel, (j) and (k) EDX spectra of BC-PEDOT-SA-PANI aerogel.

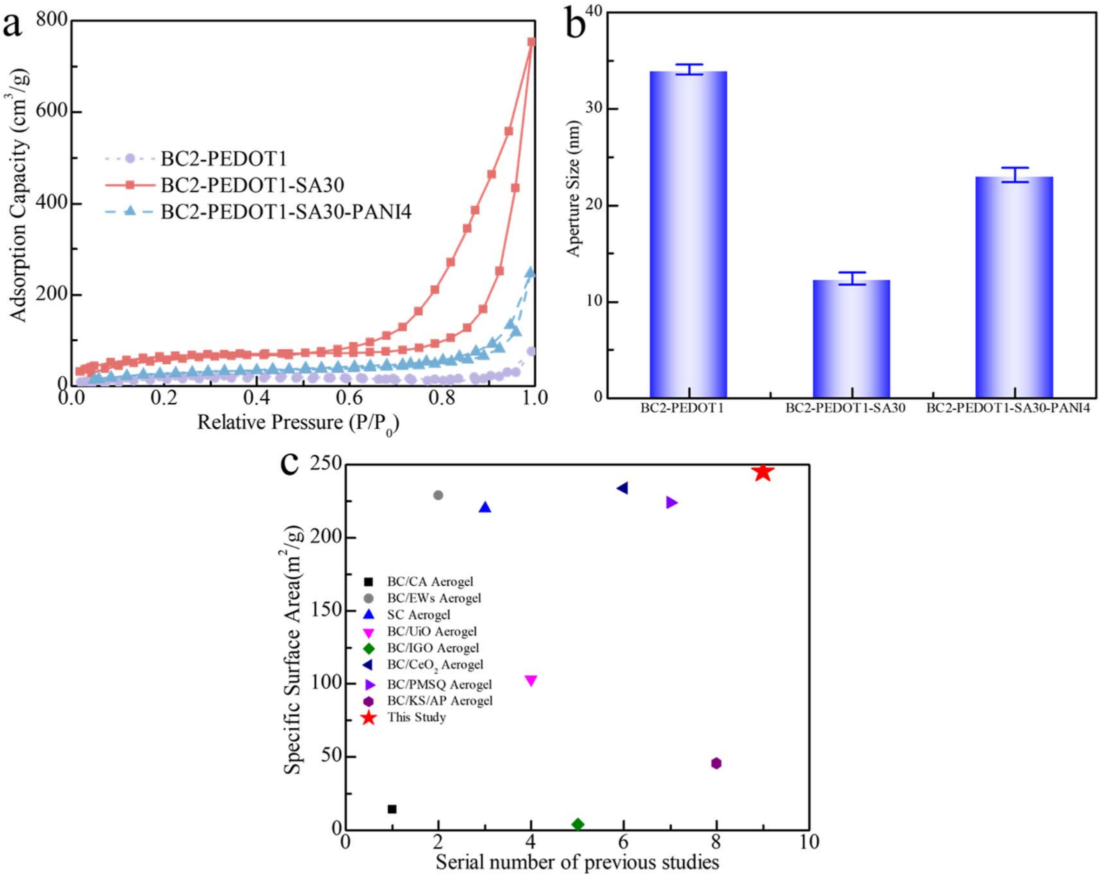

Fig. 3 (a) Adsorption–desorption isotherms, (b) average pore size, (c) comparison with previous studies (1. Lu *et al.* 2024; 2. Wei *et al.* 2025; 3. Milica *et al.* 2024; 4. Dai *et al.* 2023; 5. Ou *et al.* 2025; 6. Nina *et al.* 2023; 7. Yu *et al.* 2026; 8. Dai *et al.* 2025; 9. This study).

$$C_{\mathrm{m}} = \frac{I_{\mathrm{d}} \times \Delta t}{\Delta V \times m} \tag{2}$$

$$E = \frac{C_{\mathrm{m}} \times \Delta V^2}{7.2} \tag{3}$$

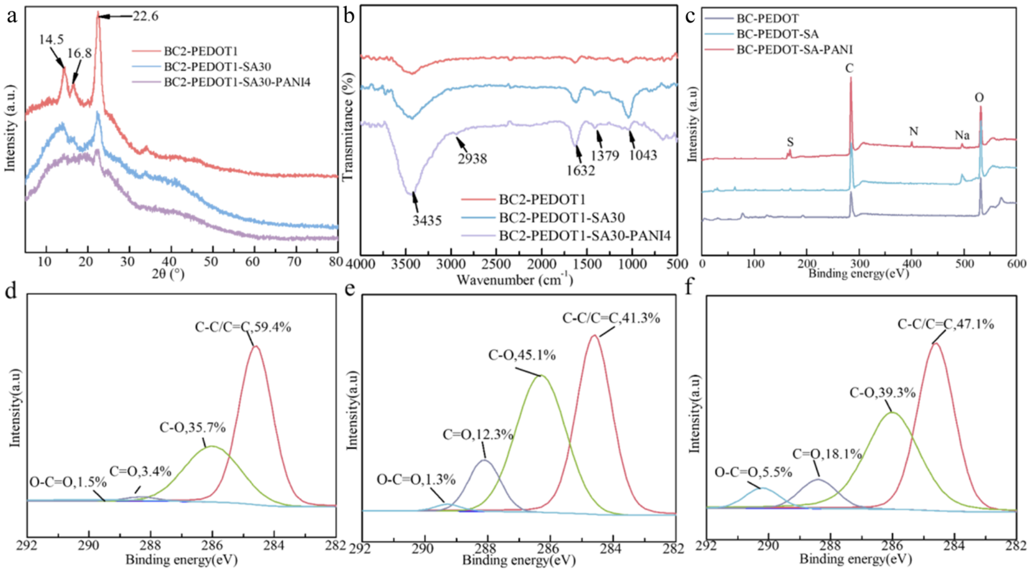

Fig. 4 (a) XRD spectra of aerogels, (b) FTIR spectra of aerogels, (c) XPS survey spectra of aerogels; (d) C 1s spectra of BC-PEDOT aerogel; (e) C 1s spectra of BC-PEDOT-SA aerogel; (f) C 1s spectra of BC-PEDOT-SA-PANI aerogel.

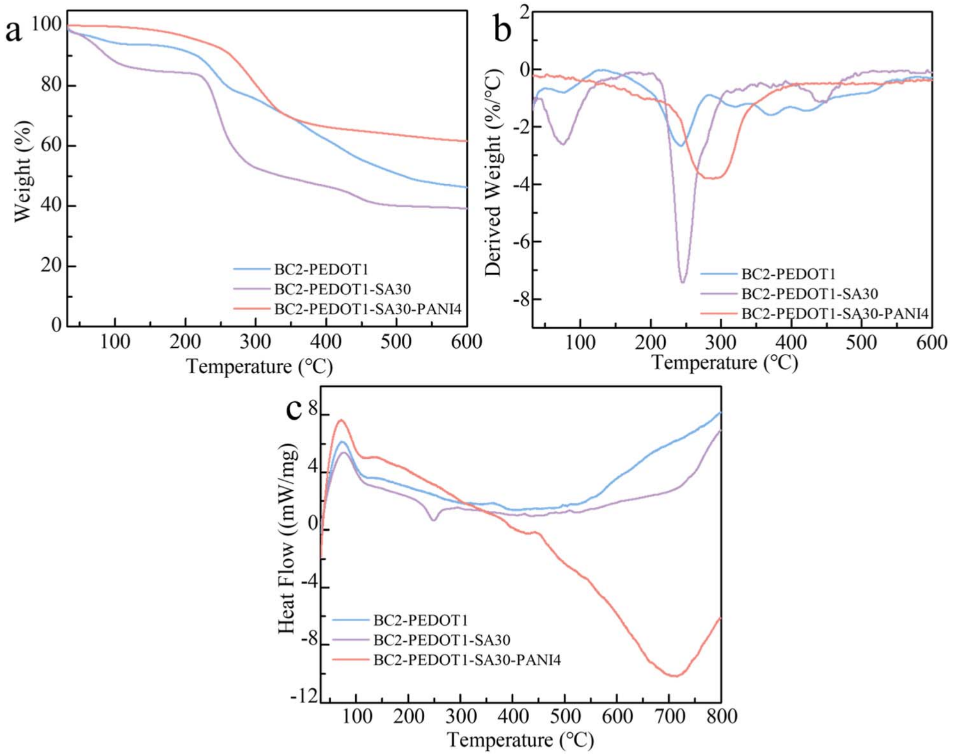

Fig. 5 (a) Thermogravimetric (TGA) curve of aerogels, (b) derivative thermogravimetric (DTG) curve, (c) differential scanning calorimetry (DSC) curve.

$$P = 3600 \times \frac{E}{\Delta t} \tag{4}$$

where C_m is the gravimetric specific capacitance, F g^{-1}; I_d is the discharge current, A; Δt is the discharge time, s; ΔV is the voltage window, V; m is the total mass of active materials, g; E is the energy density, W h kg^{-1}; P is the power density, W kg^{-1}.

A Keithley 6514 electrometer was used to measure the voltage and current of aerogels under different temperature differentials and applied pressures. Aerogel samples were connected to the electrometer's red and black probes at equal distances, and the voltage and current of the composite aerogel were measured under identical experimental conditions.

The thermoelectric test was conducted using a cold and hot stage for temperature control, and a thermocouple monitored the temperature difference between the cold and hot ends. Five temperature differences of 5 K, 10 K, 15 K, 20 K, and 25 K were applied across the sample. The aerogel's length, width, and thickness were approximately 2 cm, 1 cm, and 0.5 cm, respectively. The voltage and current of the aerogel were recorded to investigate its temperature response characteristics. Apply

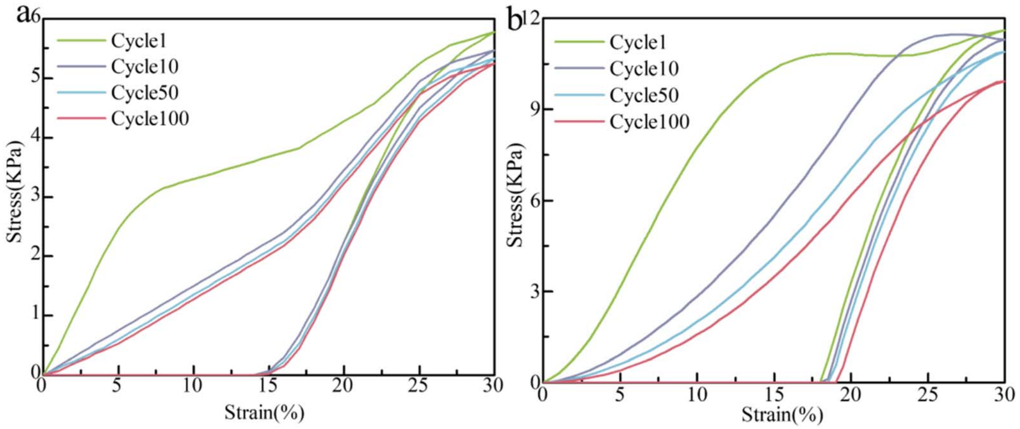

Fig. 6 (a) Cyclic compressive stress–strain curves of BC-PEDOT aerogels, (b) cyclic compressive stress–strain curves of BC-PEDOT-SA-PANI aerogels.

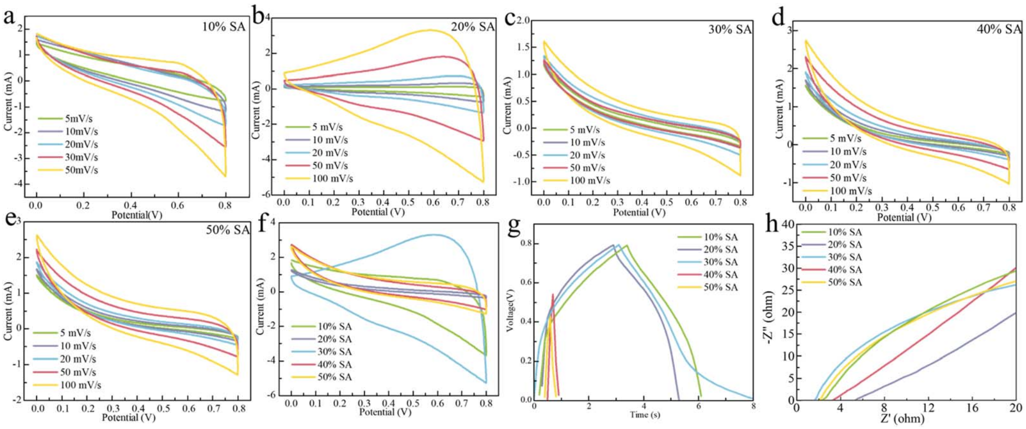

Fig. 7 (a) CV curves of aerogels with 10% SA, (b) CV curves of aerogels with 20% SA, (c) CV curves of aerogels with 30% SA, (d) CV curves of aerogels with 40% SA, (e) CV curves of aerogels with 50% SA, (f) CV curves of aerogels with different contents of SA, (g) GCD curves, (h) EIS curves.

pressures of 0.5 kPa, 1 kPa, 2 kPa, 3 kPa, and 5 kPa to the composite aerogel surface. Record the voltage and current of the composite aerogel to investigate its pressure load response patterns.

Results and discussion

Surface morphology analysis of aerogel

The SEM and EDX images of the aerogels are shown in Fig. 2. As shown in Fig. 2a and b, the pristine BC-PEDOT aerogel exhibits an open, wrinkled porous architecture, which evolves toward a more enclosed pore structure upon the introduction of SA to

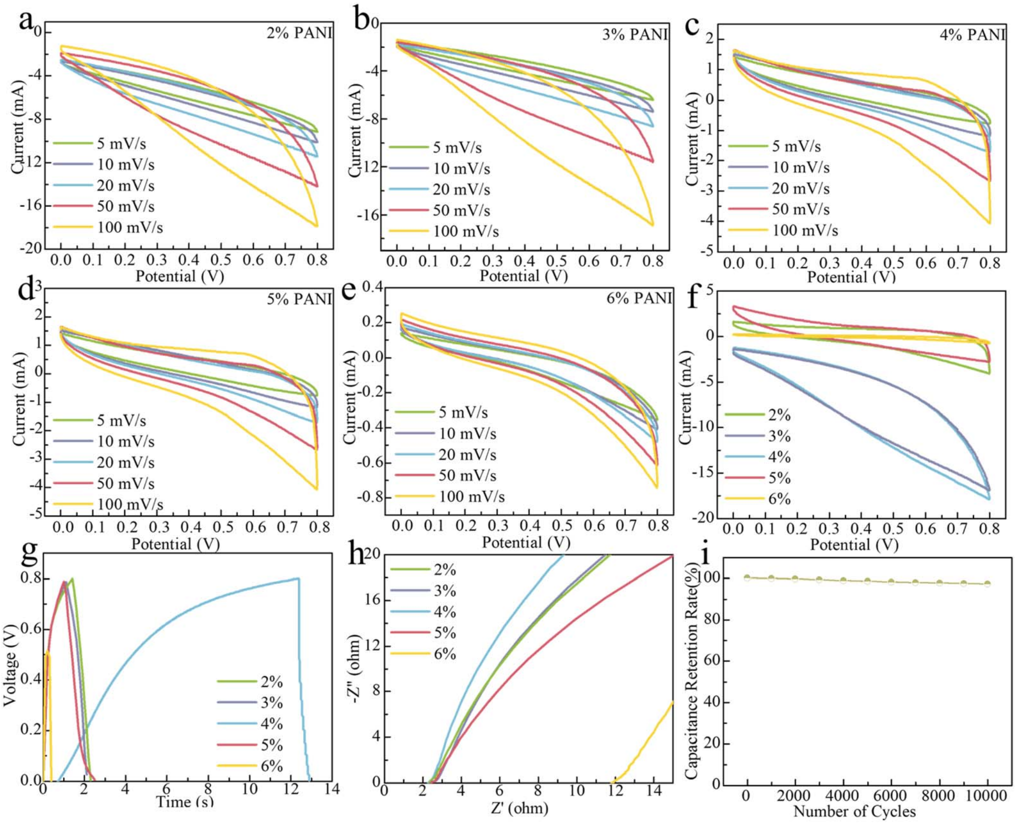

Fig. 8 (a) CV curves of aerogel with 2% PANI, (b) CV curves of aerogel with 3% PANI, (c) CV curves of aerogel with 4% PANI, (d) CV curves of aerogel with 5% PANI, (e) CV curves of aerogel with 6% PANI, (f) CV curves of aerogels with PANI, (g) GCD curves, (h) EIS curves, (i) capacitance retention rate.

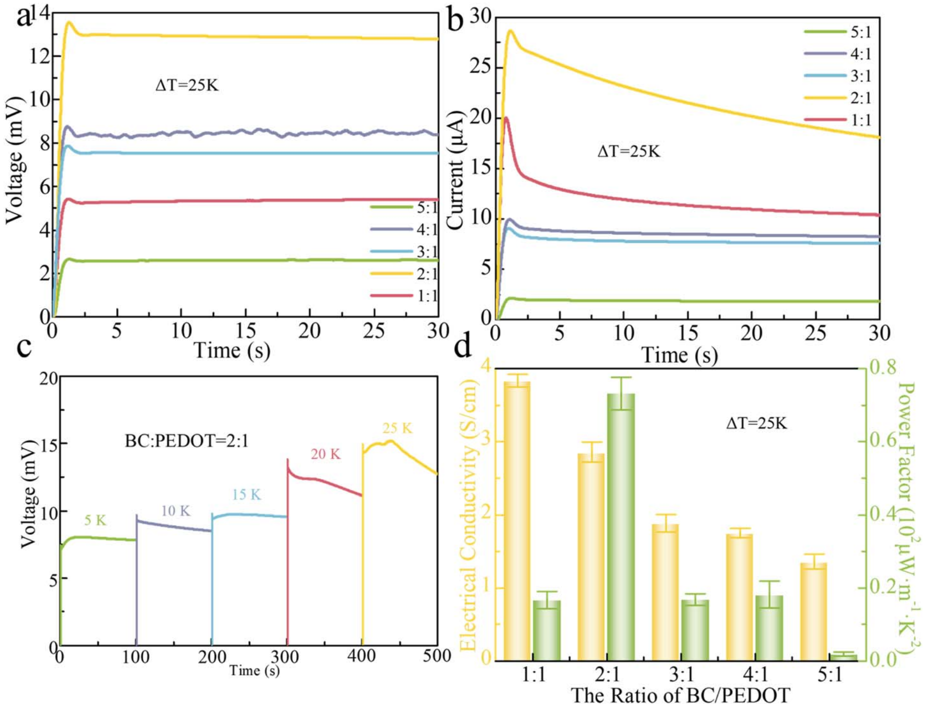

Fig. 9 (a) Output voltage of BC-PEDOT aerogels, (b) output current of BC-PEDOT aerogels, (c) temperature response of voltage, (d) electrical conductivity and power factor.

form the BC-PEDOT-SA composite aerogel. Notably, the subsequent addition of PANI in the BC-PEDOT-SA-PANI aerogel (illustrated in Fig. 2c and d), which possesses a compact, well-defined closed pore network. Fig. 2e further reveals that the PANI-based polymer component is uniformly dispersed as discrete granular nanostructures throughout the aerogel

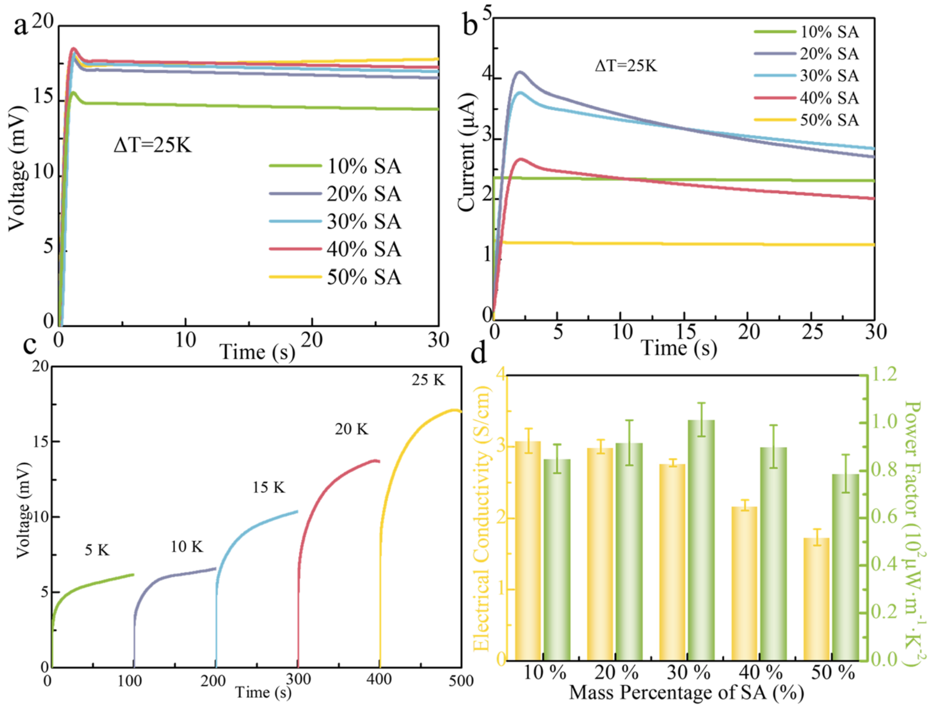

Fig. 10 (a) Output voltage of BC2-PEDOT1-SA aerogels, (b) output current of BC2-PEDOT1-SA aerogels, (c) temperature response of voltage, (d) electrical conductivity and power factor.

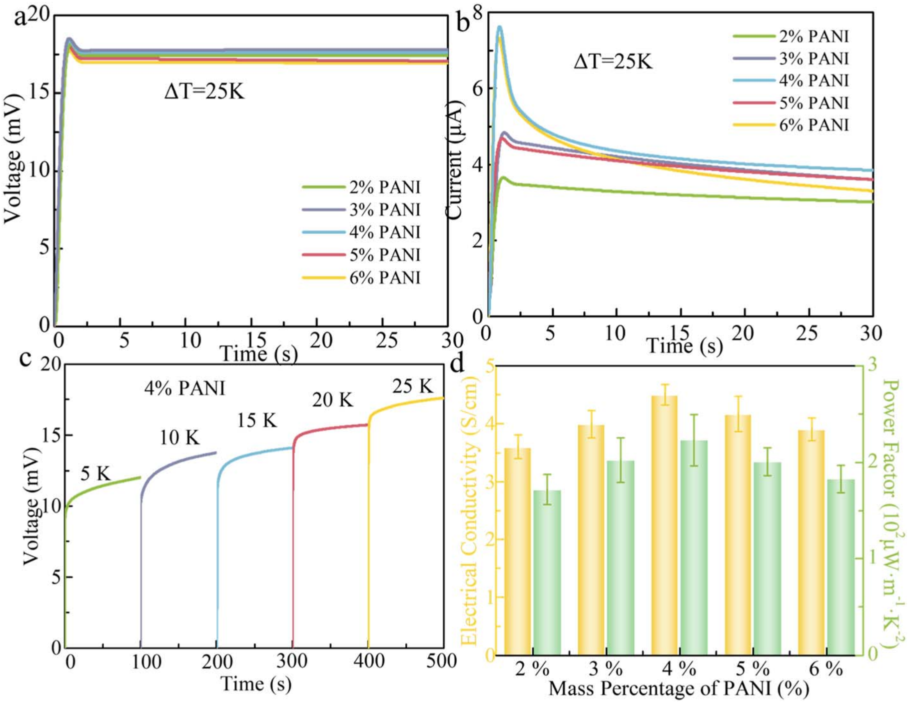

Fig. 11 (a) Output voltage of BC2-PEDOT1-SA30-PANI aerogels, (b) output current of BC2-PEDOT1-SA30-PANI aerogels, (c) temperature response of voltage of BC2-PEDOT1-SA30-PANI4 aerogel, (d) electrical conductivity and power factor of BC2-PEDOT1-SA30-PANI aerogels.

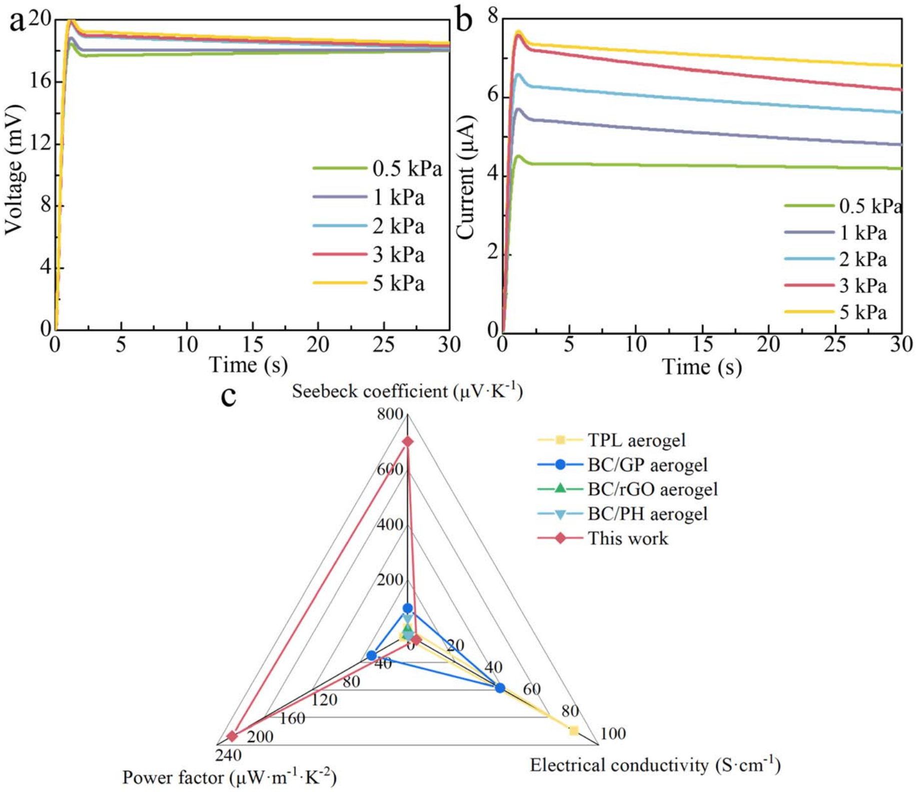

Fig. 12 (a) Output voltage under pressure, (b) current under pressure, (c) comparison with previous studies (1. Sun *et al.* 2025; 2. Nie *et al.* 2025; 3. He *et al.* 2025; 4. Essadiki *et al.* 2025).

framework, indicating effective integration of the conductive polymer into the porous network without significant agglomeration. Corresponding EDX elemental mappings (Fig. 2f–i) confirm the homogeneous distribution of C, N, Na, and S throughout the composite BC-PEDOT-SA-PANI aerogel, while the EDX spectrum (Fig. 2j) and quantitative elemental analysis (Fig. 2k; weight percentages: C 60.37%, N 2.41%, O 27.27%, Na 3.94%, S 6.01%) verify the coexistence of BC, PEDOT, SA, and PANI moieties, thereby validating the successful fabrication of the BC-PEDOT-SA-PANI composite aerogel.

Pore structure analysis of aerogels

The pore structures of BC2-PEDOT1, BC2-PEDOT1-SA30, and BC2-PEDOT1-SA30-PANI4 aerogels are systematically characterized *via* nitrogen adsorption–desorption testing (BET/BJH model), as depicted in Fig. 3. The results reveal that their isothermal adsorption curves all exhibited typical type IV characteristics. The steep increase in adsorption in the low-pressure region ($p/p_0 < 0.1$) is attributed to micropore filling. The progressive adsorption in the medium-pressure region ($0.1 \leq p/p_0 \leq 0.8$) indicates the dominant role of mesoporous monolayer-multilayer adsorption mechanisms. In contrast, capillary condensation in the high-pressure region ($p/p_0 \geq 0.8$) further confirms the connectivity of the mesoporous structure and the broad pore-size distribution. The specific surface area (SSA) calculated by the BET method indicates that introducing SA increased the aerogel SSA from 84.07 $m^2\ g^{-1}$ to 244.93 $m^2\ g^{-1}$ (a 191% increase), primarily due to the formation of a nanoscale open-pore network *via* crosslinking between SA chains and the matrix. Subsequent PANI loading reduces the SSA to 118.32 $m^2\ g^{-1}$, yet it remains higher than that of the pristine system, due to the packing of PANI within the mesopores. The average pore diameter (D_{ave}) calculated *via* the BJH model revealed that SA addition sharply reduces D_{ave} from 34.48 nm to 12.99 nm, indicating optimization toward smaller mesopores. Following PANI loading, D_{ave} rebounds to 23.09 nm, likely due to localized pore expansion caused by selective deposition within the channels. Fig. 3c compares our BET results with literature values, demonstrating that BC-PEDOT-SA-PANI aerogel achieves superior SSA (244.93 $m^2\ g^{-1}$) compared to previously reported aerogels (4.11–233.72 $m^2\ g^{-1}$).

Structural analysis of aerogels

XRD pattern in Fig. 4a shows characteristic diffraction peaks at 14.5°, 16.8°, and 22.6° for the BC2-PEDOT1 aerogel, corresponding to the (101), $(10\bar{1})$, and (002) crystal planes of bacterial cellulose I-type crystals, indicating a typical cellulose I-type crystal structure. Using the peak deconvolution method described in formula (1), the apparent crystallinity indexes of BC2-PEDOT1, BC2-PEDOT1-SA30, and BC2-PEDOT1-SA30-PANI4 aerogels are 30.4%, 16.5%, and 11.9%, respectively. Upon introduction of SA, the BC2-PEDOT1-SA30 aerogel exhibits a reduced peak intensity and broadened peak shape, accompanied by a decrease in apparent crystallinity index. This is attributed to the weakening of hydrogen-bonding interactions between the amorphous segments of SA and the BC molecular chains, thereby disrupting the regularity of the original crystalline structure. Further loading with PANI results in broadened doughnut-shaped peaks in the XRD pattern of the BC-PEDOT1-SA30-PANI4 composite aerogel. In contrast, the peak positions remain consistent with bacterial cellulose. This indicates that the introduction of amorphous PANI does not alter the interplanar spacing of the crystals but merely reduces the overall crystalline order through physical packing. FTIR spectroscopy (Fig. 4b) analysis indicates that the strong absorption band at 3435 cm^{-1} in BC2-PEDOT1 aerogel originates from the stretching vibration of the hydroxyl group (–OH) in the BC molecular chains. The absorption band at 2938 cm^{-1} corresponds to the stretching vibration of the C–H group, while those at 1632 cm^{-1} and 1379 cm^{-1} are attributed to the aromatic ring backbone vibration and the C–N group stretching vibration in the PEDOT molecule, respectively, while 1043 cm^{-1} reflects the C–O–C group vibration between BC glucose units. After SA addition, the absorption band intensities at 3435 cm^{-1} and 1632 cm^{-1} increased, confirming the strengthening of the hydrogen bond network between the abundant hydroxyl groups in SA molecules and BC2-PEDOT1. After loading PANI, the stronger characteristic peak at 3435 cm^{-1} originates from the N–H bond stretching vibration absorption on the PANI, indicating that PANI is uniformly distributed throughout the aerogel matrix.

XPS spectra of aerogels are shown in Fig. 4c–f. The XPS survey spectra (Fig. 4c) confirm that all three aerogels exhibit characteristic peaks of C 1s, O 1s, and S 2p (unique to PEDOT). The emergence of a Na signal after SA incorporation and a distinct N1s peak upon PANI introduction verifies the successful integration of each component. Deconvolution of the C 1s spectra (Fig. 4d–f) reveals: in the BC-PEDOT sample, the C–C/C=C component accounts for 59.4%, corresponding to the conjugated thiophene backbone of PEDOT and alkyl carbons of BC. Upon SA incorporation, the relative fractions of C–O (35.7% → 45.1%) and C=O (3.4% → 12.3%) increase significantly, originating from the abundant hydroxyl and carboxyl groups in SA. The ionized $-COO^-$ moieties of SA electrostatically interact with positively charged $PEDOT^+$ chains, reducing the electron cloud density of PEDOT, enhancing interfacial polarization, and suppressing PEDOT aggregation. Further introduction of PANI elevates the C–C/C=C fraction to 47.1% (attributed to the conjugated benzene/quinone rings of PANI), while the C–O fraction decreases to 39.3% and the total C=O/O–C=O fraction rises to 23.6%. These changes indicate that PANI and PEDOT form an interpenetrating network *via* π–π conjugation stacking, accompanied by intermolecular charge transfer (from PANI to PEDOT), thereby establishing continuous electron transport pathways and synergistically amplifying the interfacial effects and electronic conductivity of the aerogel.

Thermal stability analysis and mechanical performance of aerogels

Thermogravimetric analysis (TGA) and derivative thermogravimetry (DTG) are used to evaluate the thermal behavior of BC2-PEDOT1, BC2-PEDOT1-SA30, and BC2-PEDOT1-SA30-

PANI4 aerogels, as illustrated in Fig. 5. All samples exhibit a multi-step weight-loss process. The initial mass loss at low temperatures is primarily attributed to the removal of physically adsorbed/bound water from the porous polysaccharide network. In particular, BC2-PEDOT1-SA30 shows a relatively higher low-temperature weight loss, consistent with the enhanced water-binding capability of alginate and the presence of a Ca^{2+}-mediated ionically cross-linked SA network. To quantify thermal stability and avoid ambiguity from moisture loss, $T_{5\%}$ (temperature at 5% weight loss) and the maximum decomposition temperature ($T_{\max}$; DTG peak) are used. BC2-PEDOT1 exhibits $T_{5\%} = 85.8$ °C and $T_{\max} = 227.4$ °C, with a char yield of 46.1% at 600 °C. After introducing SA, $T_{5\%}$ slightly increases to 96.5 °C, and $T_{\max}$ shifts to 247.7 °C. At the same time, the char yield decreases to 39.2%, indicating that SA incorporation alters the degradation pathway and reduces the final carbonaceous residue under the tested conditions. Notably, incorporating PANI significantly enhances the high-temperature robustness: BC2-PEDOT1-SA30-PANI4 aerogel shows markedly higher $T_{5\%}$ and $T_{\max}$ values (219.3 and 289.6 °C, respectively) together with the highest char yield (61.6%), which can be attributed to the contribution of the conjugated polymer to carbonization and the more integrated composite network that restricts chain mobility during pyrolysis.

The cyclic compressive stress–strain curves of BC2-PEDOT1 and BC2-PEDOT1-SA30-PANI4 aerogels are illustrated in Fig. 6a and b. For BC2-PEDOT1 aerogel (Fig. 6a), the first cycle exhibits a typical three-stage response: an initial linear elastic region at low strain (<5%), a gradual stress plateau from ∼5% to ∼15% strain corresponding to pore wall buckling and network deformation, and a sharp stress rise in the densification region above 20% strain, with a maximum stress of ∼5.8 KPa at 30% strain. With increasing cyclic loading (1 to 100 cycles), the maximum compressive stress at 30% strain shows a moderate ∼10.3% reduction, accompanied by a slight increase in residual strain (<2% after 100 cycles), indicating good elastic recovery and moderate fatigue resistance, attributed to the reversible hydrogen-bonded BC nanofiber network and PEDOT chain entanglement, with only minor irreversible bond breakage during cycling. In contrast, BC2-PEDOT1-SA30-PANI4 aerogel (Fig. 6b) demonstrates significantly enhanced mechanical performance: the first cycle achieves a maximum stress of ∼11.5 kPa at 30% strain, nearly double that of the BC2-PEDOT1 aerogel, with an extended plateau region up to ∼18% strain, confirming improved compressive strength and structural rigidity from the dual-crosslinked network formed by additional hydrogen bonding and electrostatic interactions between SA, PANI, and BC, as well as PANI's reinforcing effect as a rigid filler. While BC2-PEDOT1-SA30-PANI4 aerogel exhibits a slightly larger ∼13.0% stress reduction after 100 cycles and a marginally higher residual strain (∼3%), its absolute stress retention and energy dissipation capacity (evidenced by persistent large hysteresis loops) remain far superior to BC2-/PEDOT1 aerogel. Overall, the incorporation of SA and PANI effectively reinforces the aerogel skeleton, endowing the multi-component aerogel with enhanced compressive strength, energy absorption, and long-term cyclic stability.

Electrochemical performance analysis

Fig. 7 shows the CV, GCD, and EIS curves of aerogels with different SA mass fractions (relative to BC). As shown in Fig. 7a–e, the CV curves exhibit nearly rectangular characteristics, indicating excellent capacitive reversibility of the aerogels. As the scan rate increases, the closed area of the CV curve increases linearly while maintaining stable morphology, confirming enhanced electron and ion transport rates and good conductivity. Calculation of the specific capacitance *via* integration (Fig. 7f) reveals that the aerogel with 30% SA reaches a maximum of mass-specific capacitance of 33.75 F g^{-1}. This represents improvements of 142%, 705%, 453%, and 344% over other compositions (10%, 30%, 40%, and 50%), attributed to the synergistic effect of an optimized pore structure and conductive pathways at moderate SA content. The GCD curve in Fig. 7g exhibits an approximately symmetrical triangular shape with no significant voltage drop, indicating a coulombic efficiency close to 100%. The 30% SA composition demonstrated the longest discharge time, further validating its high charge storage capacity. EIS analysis in Fig. 7h reveals that the aerogel's equivalent series resistance (R_s) first decreases and then increases with SA content, reaching a minimum of 1.75 Ω at 30% SA. This stems from moderate crosslinking between the SA molecular chains and PEDOT, forming a low-impedance conductive network. Ca^{2+} crosslinking creates a dual-functional network. Therefore, ionic-conducting pathways reduce interfacial resistance from 5.76 Ω to 1.75 Ω. Conversely, excessively high SA content (>30%) causes the aggregation of insulating polysaccharide chains, disrupting the continuity of the conductive phase and significantly increasing R_s, reaching 5.76 Ω at 50% SA. Based on electrochemical test results, at an SA mass fraction of 30%, the aerogel achieves a high specific capacitance of 33.75 F g^{-1}, nearly 100% coulombic efficiency, and a low internal resistance of 1.75 Ω through synergistic optimization of its pore structure, conductive network, and interfacial impedance.

Fig. 8 shows the CV, GCD, and EIS curves of composite aerogels with different PANI mass fractions. The CV curves shown in Fig. 8a–e reveal that the integral areas of all aerogel samples increase linearly with scan rate from 10 mV s^{-1} to 100 mV s^{-1}, indicating diffusion-controlled capacitive behavior and favorable ion-transport kinetics. Among them, the CV integral area reached its maximum at a PANI mass fraction of 4%, corresponding to a mass-specific capacitance of 37.09 F g^{-1}. This is attributed to the moderate PANI content, which optimizes the synergistic effect between the conductive network and the pseudocapacitive active sites. GCD testing in Fig. 8g reveals that all component curves were nearly symmetrical triangles, with minimal IR drop and coulombic efficiency approaching 100%. The 4% PANI component exhibits the longest discharge time, further validating its outstanding charge-storage capability. EIS analysis in Fig. 8h reveals that the aerogel's equivalent series resistance (R_s) initially increases and then decreases with increasing PANI content, reaching a minimum of 2.28 Ω at 4% PANI. This stems from the low-impedance conductive pathways formed by π–π conjugated structures and hydrogen bonding between PANI and the BC-PEDOT matrix. However, when PANI content exceeds 4%, the accumulation of insulating oxidation products disrupts the conductive network, leading to a significant increase in R_s. Integrating the electrochemical test results, at a PANI mass fraction of 4%, the composite aerogel achieves optimal ion transport efficiency and energy storage performance through the synergistic effects of an optimized conductive network, maximized pseudocapacitive active sites (37.09 F g^{-1}), and nearly 100% coulombic efficiency. Fig. 8i shows a capacitance retention of 98.3% after 10 000 cycles.

Power generation performance

Fig. 9 shows the temperature responses of voltage, current, and capacitance, as well as variations in electrical conductivity and power factor, for aerogels with different BC-PEDOT ratios. As shown in Fig. 9a and b, the voltage signals of all aerogel samples under a 25 K temperature difference stabilize rapidly within 2–3 s. When the ratio of BC to PEDOT is 2 : 1, the aerogel exhibits a voltage of 12.7 mV and a current of 17.8 μA. This phenomenon is attributed to PEDOT, a conductive polymer, which introduces additional charge carriers into the aerogel system as its content increases. This creates a richer network of conductive pathways within the aerogel, leading to more continuous electron-transport paths.

As shown in Fig. 9c, the response voltage of the BC2-PEDOT1 aerogel increases with the temperature difference. At a temperature difference of 25 K, the output voltage reaches 12.7 mV. Using the Seebeck coefficient formula $S = \Delta V/\Delta T$ (where S is the Seebeck coefficient, ΔV is the voltage difference, and ΔT is the temperature difference), the Seebeck coefficient is calculated as 0.51 mV K^{-1}. This indicates that the BC2-PEDOT1 aerogel exhibits a pronounced thermoelectric effect, capable of converting thermal energy into electrical energy, and that its thermoelectric conversion performance is positively correlated with the temperature difference. Fig. 9d shows that the electrical conductivity of the aerogels gradually increases with increasing PEDOT content. And the BC2-PEDOT1 aerogel exhibits optimal thermoelectric performance, with a power factor of 72.8 μW m^{-1} K^{-2}. This occurs because the three-dimensional framework of BC ensures uniform dispersion of PEDOT, preventing agglomeration that would decrease conductivity. At the same time, a sufficient amount of PEDOT is provided to provide an adequate number of charge carriers, achieving a balance between conductivity and the Seebeck coefficient and thus the optimal power factor.

Fig. 10a and b shows the voltage and current response characteristics of the aerogel at different SA mass fractions. At approximately 2 seconds, the aerogel's voltage and current responses stabilize as the SA mass fraction increases. As the amount of sodium alginate increases, the output voltage gradually increases, while the output current first increases and then decreases. At a sodium alginate concentration of 50%, the output voltage reaches a maximum of 17.8 mV. At a sodium alginate concentration of 30%, the output current is the highest, at 2.8 μA. This is because the addition of sodium alginate may have altered the effective doping state and charge compensation of PEDOT, thereby decreasing the carrier concentration and increasing the Seebeck coefficient. Fig. 10c illustrates the voltage response of the BC2-PEDOT1-SA30 aerogel to temperature differences. As the temperature difference increases, the response voltage of the BC2-PEDOT1-SA30 aerogel gradually increases. At a temperature difference of 25 K, the aerogel exhibits an output voltage of 17 mV and a Seebeck coefficient of 0.68 mV K^{-1}. Fig. 10d shows that as the SA mass fraction increases, the electrical conductivity of aerogels gradually decreases, while the power factor first increases and then decreases. When the SA mass fraction is 30%, the aerogel's power factor is 101.3 μW m^{-1} K^{-2}. The band doping and interface regulation induced by SA/Ca^{2+} enhance the Seebeck coefficient (even as energy filtering is strengthened). At low concentrations, this is supported by the increased PEDOT content and the improved permeability and connectivity resulting from the stable structure. In contrast, at high concentrations, the insulating cross-linking phase fragments the conductive network. It enhances interface scattering, causing electrical conductivity to decrease rapidly and ultimately dominating the decline in power factor.

Fig. 11 shows the voltage, current, and temperature responses of the electrical conductivity and power factor of BC2-PEDOT1-SA30-PANI composite aerogels with different PANI mass fractions. As shown in Fig. 11a and b, the electrical properties of the composite aerogels reach a steady state after approximately 1 s of transient fluctuation. As the PANI content increases, the output voltage initially rises and then decreases slightly. This is because $V = S \times \Delta T$. The heterogeneous interface energy filtering introduced by PANI, along with a slight increase in the local doping state, results in a modest increase in the Seebeck coefficient. However, when the PANI content is high, the increase in carrier concentration and the weakening of energy filtering due to phase separation result in a decrease in the Seebeck coefficient. As the PANI content increases, the output current first increases and then decreases. This is because at low PANI content, it primarily enhances the connectivity of the conductive network, whereas at high PANI content, agglomeration/interfacial scattering, and "bottlenecking" of pathways cause the effective conductivity to plateau or even decrease, resulting in reduced current. Analysis of the temperature-response characteristics, as shown in Fig. 11c, indicates that the composite aerogel's response voltage increases with temperature. At a temperature difference of 25 K, the BC2-PEDOT1-SA30-PANI4 aerogel exhibits an output voltage of 17.6 mV and a Seebeck coefficient of 0.7 mV K^{-1}. The electrical conductivity and power factor, as shown in Fig. 11d, further validate the regulatory role of PANI content on the composite system's electrical properties. Both electrical conductivity and power factor initially increase and then decrease as the PANI mass fraction increases, reaching optimal values at 4% (electrical conductivity: 4.5 S cm^{-1}; power factor: 220.5 μW m^{-1} K^{-2}). This is because the doped PANI forms a parallel conducting path with PEDOT, thereby enhancing the flow connectivity. However, at high concentrations, it leads to microphase separation, increased interfacial resistance, and carrier scattering, which decrease mobility and offset the gain in the conducting phase. From Fig. 12c, it can be indicated that the thermoelectric performance of the composite aerogels by this study is better than that of other aerogels as reported in the previous literature.[16–19]

Fig. 12a and b shows the voltage and current responses of the BC2-PEDOT1-SA30-PANI4 composite aerogel under different pressures (the stress test was conducted at room temperature, 25 °C, with no additional temperature difference). As shown in Fig. 12a and b, the response voltage and current change rapidly with pressure, stabilizing within approximately 2 s. As the pressure increased, the aerogel's voltage rose only slightly. And the current gradually increased. Under a 5 kPa pressure load, its voltage and current responses remained stable at 18.5 mV and 6.8 μA, respectively, demonstrating good pressure-sensitive characteristics. This is because pressure-induced densification of the aerogel's pore structure and increased contact points within the conductive framework reduce interface contact resistance, resulting in a significant decrease in the equivalent internal resistance.

Conclusions

This study combined freeze-drying with the preparation of BC-PEDOT-SA-PANI composite aerogels and systematically investigated the mechanism underlying the structure–property synergy of these aerogels. SA increased the specific surface area, while PANI controlled the pore-size distribution, forming a multi-level pore system. The aerogel exhibited excellent thermal stability, with the initial decomposition temperature elevated to 219.3 °C and the maximum weight loss reduced to 38.4%, thereby improving its practicality and durability. At a BC : PEDOT mass ratio of 2 : 1, with SA (30%) and PANI (4%), the composite aerogel achieved a mass-specific capacitance of 37.09 F g^{-1}. After 10 000 cycles, the capacitance retention reached 98.3%, demonstrating outstanding rate capability and cycling stability. At a temperature difference of 25 K, the composite aerogel exhibited a Seebeck coefficient of 0.7 mV K^{-1}, an electrical conductivity of 4.5 S cm^{-1}, and a power factor of 220.5 μW m^{-1} K^{-2}, indicating highly efficient thermoelectric conversion. Under pressure (5 kPa), the composite aerogel exhibits stable voltage (18.5 mV) and current (6.8 μA) responses, demonstrating good pressure-sensitive characteristics. The composite aerogel exhibits good mechanical properties, with a stress of up to 9.6 kPa at 100% compressive deformation after 100 cycles. These remarkable properties, combined with enhanced thermal stability and mechanical robustness, position these aerogels as promising candidates for diverse applications, including self-powered sensors in smart textiles, flexible energy storage devices, thermal warning systems in firefighting clothing, and pressure-sensitive human–machine interfaces.

Author contributions

All authors contributed to the conception and design of the study. Material preparation was performed by Qi Xiao and Enhao Xie. Analyses were performed by Zhe Gao, and Ulugbek Gulbaev. Conceptualization was performed by Wei Fan and Jahongir Akhmedov. Data collection was performed by Wen Chen and Yuhan Wang. The first draft of the manuscript was written by Qi Xiao, and all authors commented on earlier versions. All authors read and approved the final manuscript.

Conflicts of interest

The authors declare no relevant financial or non-financial interests.

Data availability

All data generated or analyzed during this study are included in this article.

Acknowledgements

This work was supported by the National Natural Science Foundation of China (52403032), Natural Science Foundation of the Jiangsu Higher Education Institutions of China (23KJD540001), Key Laboratory of Functional Textile Material and Product, Ministry of Education (2024FTMP006); Science and Technology Guidance Project of China National Textile and Apparel Council (2025019).

References

1 Z. Wang, B. Sun, X. Jin, C. Chen and D. Sun, Multifunctional bacterial cellulose-based aerogel with tunable mechanical property for filtration and thermal insulation, *Int. J. Biol. Macromol.*, 2025, **308**, 142499.

2 J. Wang, L. Liu, W. Dong, J. Tao, R. Fu, Y. Liu, X. Yang, H. Yu and H. Sai, Ultra-High Radial Elastic Aerogel Fibers for Thermal Insulation Textile, *Adv. Funct. Mater.*, 2025, **35**, 17873.

3 M. Liu, R. Chu, G. Li, Z. Song, D. Yu, H. Wang, H. Liu and W. Liu, Hydrogel-infiltrated micropatterned nano-carbon aerogel sheet composed of partially carbonized cellulose nanofibers for wearable sensor, *Nano Energy*, 2025, **138**, 110852.

4 Y. Zhang, J. Wang, Q. Wu, T. Shan, S. Bai, D. Lan, B. Zhang, Y. Liu and X. Su, Enhanced electromagnetic wave absorption of bacterial cellulose/reduced graphene oxide aerogel by eco-friendly in-situ construction, *J. Colloid Interface Sci.*, 2025, **678**, 648–655.

5 S. Li, L. Luo, M. Z. Hasan, N. Shi, Q. Liu, D. Li, C. Yue, R. Zhang, S. Sha and J. Zhu, Directional fabrication of an ultra-light and porous bacterial nanocellulose/MXene composite aerogel for efficient thermal management, *Int. J. Biol. Macromol.*, 2025, **311**, 144054.

6 H. He, Y. Qin, J. Liu, Y. Wang, J. Wang, Y. Zhao, Z. Zhu, Q. Jiang, Y. Wan, X. Qu and Z. Yu, A wearable self-powered fire warning e-textile enabled by aramid nanofibers/MXene/silver nanowires aerogel fiber for fire protection used in firefighting clothing, *Chem. Eng. J.*, 2023, **460**, 141661.

7 L. Chen, J. Lou, Y. Zong, Z. Liu, Y. Jiang and W. Han, Wood-like aerogel for thermoelectric generators based on BC/PEDOT/SWCNT, *Cellulose*, 2023, **30**, 3141–3152.

8 Z. Yu, Y. Wan, M. Zhou, M. H. Mia, S. Huo, L. Huang, J. Xu, Q. Jiang, Z. Zheng, X. Hu and H. He, Muscle-Inspired Anisotropic Aramid Nanofibers Aerogel Exhibiting High-Efficiency Thermoelectric Conversion and Precise Temperature Monitoring for Firefighting Clothing, *Nano-Micro Lett.*, 2025, **17**, 214.

9 L. Tian, F.-L. Gao, Y.-X. Li, Z.-Y. Yang, X. Xu, Z.-Z. Yu, J. Shang, R.-W. Li and X. Li, High-Performance Bimodal Temperature/Pressure Tactile Sensor Based on Lamellar CNT/MXene/Cellulose Nanofibers Aerogel with Enhanced Multifunctionality, *Adv. Funct. Mater.*, 2025, **35**, 18988.

10 H. Sun, B.-X. Li, Z. Luo, M. Jin, Q. Quan, C. Ding, Z.-Z. Yu and D. Yang, Integrating and anisotropic MXene/reduced graphene oxide/PEDOT:PSS hybrid aerogel for active/passive thermal protection and stepwise thermal warning, *Chem. Eng. J.*, 2024, **496**, 153536.

11 F.-L. Gao, P. Min, Q. Ma, T. Zhang, Z.-Z. Yu, J. Shang, R.-W. Li and X. Li, Multifunctional Thermoelectric Temperature Sensor for Noncontact Information Transfer and Tactile Sensing in Human-Machine Interaction, *Adv. Funct. Mater.*, 2024, **34**, 9553.

12 Y. Wu, F. Wang, Y. Wu, B. Yan and Q. Li, Advanced ionic actuators with high-performance and high-reproducibility based on free-standing bacterial cellulose-reinforced poly(diallyldimethylammonium chloride) membranes and PEDOT/PSS electrodes, *Cellulose*, 2023, **30**, 7825–7837.

13 Y. Wu, Q. Cui, R. Qi and F. Wang, Self-standing bacterial cellulose-reinforced poly(3,4-ethylenedioxythiophene)/poly(4-styrenesulfonate) doped with graphene oxide composite electrodes for high-performance ionic electroactive soft actuators, *Nanoscale Adv.*, 2024, **6**, 2209–2216.

14 X. He, M. Liu, J. Cai, Z. Li, Z. Teng, Y. Hao, Y. Cui, J. Yu, L. Wang and X. Qin, Waste Cotton-Derived Fiber-Based Thermoelectric Aerogel for Wearable and Self-Powered Temperature-Compression Strain Dual-Parameter Sensing, *Engineering*, 2024, **39**, 235–243.

15 V. Tran, G. Mastantuoni, J. Garemark, C. H. Dreimol, X. Wang, M. Berggren, Q. Zhou, R. Kroon and I. Engquist, Interconnecting EDOT-Based Polymers with Native Lignin toward Enhanced Charge Storage in Conductive Wood, *ACS Appl. Mater. Interfaces*, 2024, **16**, 68416–68425.

16 X. H. Sun, F. M. Wang, Y. Yu, Y. F. Liu, J. Z. Zhou, Z. S. Jiang, Y. D. Li, H. Y. Yang and C. Y. Wang, In-situ polymerized tourmaline/polypyrrole/lignocellulose aerogel for flame-resistant and intelligent fire alarm sensor, *Int. J. Biol. Macromol.*, 2025, **309**, 142733.

17 Y. A. Nie, Y. Hu, N. Xin, Y. F. Li, X. Zhao, M. Zhang and G. H. Tang, Cost-effective graphite aerogel for high-temperature thermoelectrics: Synergizing ultra-high electrical conductivity and thermal insulation, *J. Colloid Interface Sci.*, 2025, **697**, 137926.

18 P. He, J. Liu, Y. Wen, N. Shao and Q. Zhang, Highly Robust 3D rGO Aerogel with Tunable Thermoelectric Effect for Multifunctional Sensing Applications, *ACS Appl. Mater. Interfaces*, 2025, **17**, 24339–24350.

19 S. Essadiki, A. Carvalho, F. Vigneron, G. Fleith, J. Combet, D. Constantin, N. Stein and L. Biniek, Efficiently doped P3HT and polystyrene blend with porous 3D structure for thermoelectric applications, *J. Mater. Chem. C*, 2025, **14**, 1056–1068.